

Computational Electrochemistry: The Simulation of Voltammetry in Microchannels with Low Conductivity Solutions

Iain E. Henley and Adrian C. Fisher*

Department of Chemistry, University of Bath, Claverton Down, Bath BA2 7AY, United Kingdom

Received: February 28, 2003; In Final Form: April 21, 2003

A numerical approach to determining the secondary current–density distribution in a new class of microelectrochemical sensors with critical dimensions in the range 20–50 μm high by 100–500 μm wide and 1–10 cm long is described. The finite element method is employed to solve the relevant fluid dynamic, mass transport, and potential distribution equations in three dimensions to reveal quantitative information on the current–voltage response. The Tafel slope of the device is calculated for a range of electrolyte conductivities from 0.001 to 0.01 $\Omega^{-1}\text{cm}^{-1}$, and the distortion in the current–voltage curves from working with low conductivity solutions is determined. The effect on the current–voltage curve of using a range of reference electrode positions is investigated, and the optimal configuration is discovered. Finally, the current–voltage response of a multi-working electrode device is calculated using a finite element simulation for a cell of dimensions 400 μm high and assumed infinite width, for a range of offset potentials.

Introduction

It has long been recognized that the current density distribution and its dependence on solution resistance, hydrodynamic conditions, and impedances associated with charge-transfer reactions is of critical importance in applications such as electrodeposition¹ and electrochemical sensing.^{2–4} For example, in the electrodeposition process used in the manufacture of integrated circuits, a nonuniform current density on an electrode will result in an uneven film thickness. In sensing applications, the current distribution has a large influence on the current–voltage response of the cell and is required to derive kinetic and mechanistic information.^{5,6} Although analytical solutions are possible for simple cell geometries, these often include large approximations and only consider idealized cases.⁷ Numerical solutions are normally used where comparison with experiment is needed, and with the increase in computer speeds and memory, it has become realistic to make codes more generalized so that they can be applied to a large range of geometries.⁸ In this study, a code is developed and applied to the determination of the current distribution in a microelectrochemical reactor (MECR).^{9–13} Specifically, a microscale channel electrode is investigated for which previous numerical calculations based on mass transport only controlled currents have produced a primary current distribution in good agreement with experiment.^{14–16} The distribution of electrical potential throughout the cell is now included in the model to allow the calculation of a secondary distribution which is more accurate for low conductivity solutions. Previous studies have shown that the resistance of the bulk electrolyte causes an ohmic drop in the potential of the solution where there is a flow of current. This deviation from the presumed constant potential situation can result in a distortion of the current–voltage curve shifting the half wave potential from the expected value and producing a potential dependent error in the Tafel slope. The extent to which this effect is present in microelectrochemical cells, which have the

advantage of passing lower currents and so can be used with more resistive electrolyte solutions is investigated.

There are a number of numerical methods that have been used to calculate current distribution of which the earliest was published in 1964 using the finite difference method (FDM). In the seventies, the finite element method (FEM) was introduced initially for structural engineering but was later adapted to heat transfer and mass transport problems and has shown advantages in stability and the ability to model curved and irregular geometries. The boundary element method (BEM) which recast the problem to one in which only boundary values need be considered was introduced later, but although significantly simplifying the task of discretising the domain and reducing the computational overhead, it currently has limitations in the range of problems which can be solved.

In this study, an approach is presented based on FEM to solve the relevant governing equations. The current-density distribution and the potential dependent error in the current–voltage curve has been calculated for a MECR with dimensions of the order 100 μm wide by 50 μm high. The cell has a working electrode (WE) of the same width as the channel, differing from the normal practice of narrowing the electrode to leave a gap at the sides.² This new geometry required the implementation of a full 3-dimensional fluid dynamic, mass transport, and potential distribution simulation because a constant fluid velocity over the whole electrode width can no longer be assumed. The FEM code discretised the channel volume into hexahedral shaped elements and solved the relevant governing equations using an iterative scheme. The code was then applied to the computer-aided design of new cell geometries by investigating the effect of the reference electrode (RE) position on the shape of the Tafel slope. A second working electrode was later added to model the potential distribution in a four electrode cell with two working electrodes at different potentials.

Channel Cell Model

The cell consists of a rectangular duct with a microband working electrode (WE) placed smoothly in one wall across

* To whom correspondence should be addressed. Fax: 44-1225-826231. E-mail: chsac@bath.ac.uk.

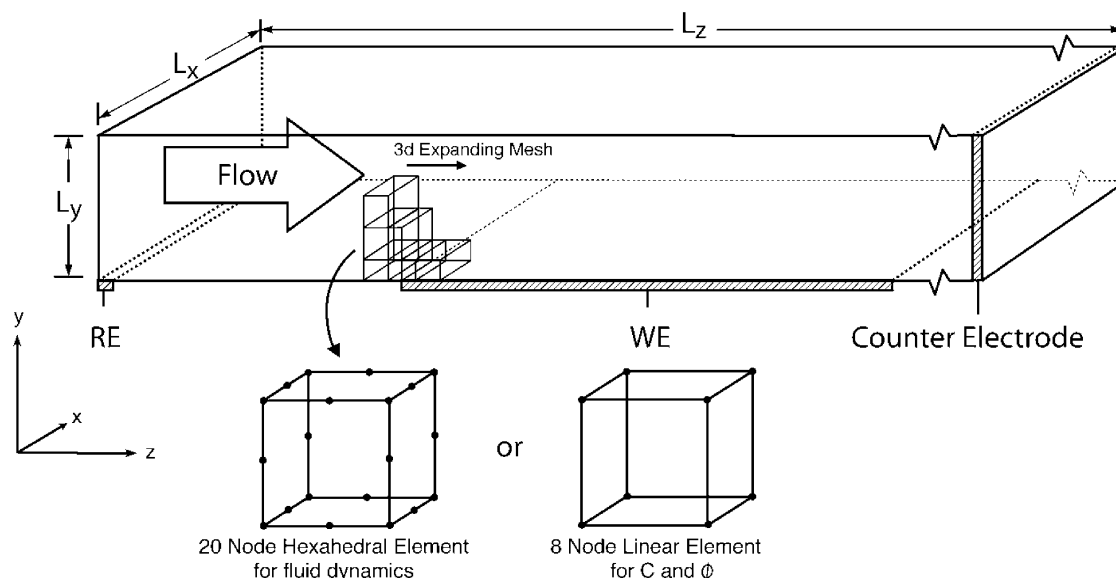


Figure 1. Geometry of the MECR with a part of the expanding mesh of hexahedral elements illustrated. The exact geometry of the expanding regions varied with each simulation.

the whole width of the channel. The counter is placed downstream of the electrode, and a reference is, in general, placed upstream though some new reference positions are investigated in this paper (Figure 1). A simple one electron-transfer redox reaction is driven at the WE



Because of the resistance of the electrolyte, the flow of current from the working to the counter, via movement of ions in the solution, causes an ohmic drop in potential. This can be modeled by the Poisson–Boltzmann equation which couples the electrolyte ion distribution to the electric field⁸

$$\nabla^2 \phi = -\frac{F}{\epsilon} \sum zc \quad (2)$$

where ϕ is the electrical potential, F is Faradays constant, ϵ is the permittivity, z is the valence, and c is the concentration. By assuming charge neutrality at every point, this can be reduced to a Laplace equation

$$\nabla^2 \phi = 0 \quad (3)$$

This assumption breaks down in regions extremely close to the electrode surface, within the Helmholtz double layer, which would result in the migration of charged species. This has not been incorporated in the model as previous work has shown good experimental agreement without including the effects of migration^{14,17–20}. At the electrode surface, the normal electric field can be related to the current density distribution, which in turn is related to the flux of reactant⁸

$$\frac{\partial \phi}{\partial n} = -\frac{i}{\kappa} = -\frac{n_e D F}{\kappa} \frac{\partial C}{\partial n} \quad (4)$$

where i is the current density, κ is the solution conductivity, n is the axis normal to the surface, n_e is the number of electrons transferred per reaction, D is the diffusion coefficient, F is Faradays constant, and C is the concentration distribution of

reactant which can be modeled with the diffusion-convection equation

$$\frac{\partial C}{\partial t} = D \nabla^2 C - \nabla(\bar{v}C) \quad (5)$$

where t is time and \bar{v} is the liquid velocity. As the finite size of the ions is not included in this model, the solution potential at the electrode surface is defined as that immediately beyond the Stern layer of ions.

For extremely fast reactions where equilibrium can be assumed, the value of C at the electrode surface is determined by the Nernst equation, assuming reactivity to be proportional to the concentration of species

$$\frac{|A|}{|B|} = \frac{C}{C^\infty - C} = \exp\left(\frac{(E - E_0)n_e F}{RT}\right) \quad (6)$$

where C^∞ is the bulk concentration of the reactant, E is the potential difference between the WE and the solution, and E_0 is the half wave potential.

The velocity field of the liquid is calculated by application of the incompressible Navier–Stokes equations^{21,22} coupled with the continuity equation and appropriate boundary conditions

$$\frac{\partial \bar{v}}{\partial t} = \frac{-\nabla p}{\rho} + \frac{\mu}{\rho} \Delta \bar{v} - (\bar{v} \nabla) \bar{v} \quad (7)$$

$$\bar{\nabla} \cdot \bar{v} = 0 \quad (8)$$

Finite Element Method

Ignoring time dependence, the velocity field was calculated from eqs 7 and 8 via FEM using an array of 20 noded hexahedral elements²³ of sufficiently small size that the solution could be approximated as the summation of a set of 20 quadratic interpolation functions $N_i(x,y,z)$ over each element

$$\bar{v}(x,y,z) = \sum_{i=1}^{20} N_i(x,y,z) \bar{v}_i \quad (9)$$

where \bar{v}_i is the velocity at the i th node of each element. The

pressure field was similarly approximated by a set of 8 linear interpolation functions $M_i(x,y,z)$

$$p(x,y,z) = \sum_{i=1}^8 M_i(x,y,z) p_i \quad (10)$$

where p_i is the pressure at the i th corner node of each element. The Galerkin weighted residual technique was then applied to formulate the Navier Stokes and continuity equations in Cartesian coordinates as a single matrix equation for each element (eq 11)

$$\begin{aligned} & \int \int \int_{V^{(e)}} \mu \left(\frac{\partial \vec{N}^T}{\partial x} \frac{\partial \vec{N}}{\partial x} + \frac{\partial \vec{N}^T}{\partial y} \frac{\partial \vec{N}}{\partial y} + \frac{\partial \vec{N}^T}{\partial z} \frac{\partial \vec{N}}{\partial z} \right) + \\ & \quad \rho \left(v_x \vec{N}^T \frac{\partial \vec{N}}{\partial x} + v_y \vec{N}^T \frac{\partial \vec{N}}{\partial y} + v_z \vec{N}^T \frac{\partial \vec{N}}{\partial z} \right) dx dy dz \cdot \vec{v}_x + \\ & \quad \int \int \int_{V^{(e)}} \vec{N}^T \frac{\partial \vec{M}}{\partial x} dx dy dz \vec{p} = 0 \\ & \int \int \int_{V^{(e)}} \mu \left(\frac{\partial \vec{N}^T}{\partial x} \frac{\partial \vec{N}}{\partial x} + \frac{\partial \vec{N}^T}{\partial y} \frac{\partial \vec{N}}{\partial y} + \frac{\partial \vec{N}^T}{\partial z} \frac{\partial \vec{N}}{\partial z} \right) + \\ & \quad \rho \left(v_x \vec{N}^T \frac{\partial \vec{N}}{\partial x} + v_y \vec{N}^T \frac{\partial \vec{N}}{\partial y} + v_z \vec{N}^T \frac{\partial \vec{N}}{\partial z} \right) dx dy dz \cdot \vec{v}_y + \\ & \quad \int \int \int_{V^{(e)}} \vec{N}^T \frac{\partial \vec{M}}{\partial y} dx dy dz \vec{p} = 0 \\ & \int \int \int_{V^{(e)}} \mu \left(\frac{\partial \vec{N}^T}{\partial x} \frac{\partial \vec{N}}{\partial x} + \frac{\partial \vec{N}^T}{\partial y} \frac{\partial \vec{N}}{\partial y} + \frac{\partial \vec{N}^T}{\partial z} \frac{\partial \vec{N}}{\partial z} \right) + \\ & \quad \rho \left(v_x \vec{N}^T \frac{\partial \vec{N}}{\partial x} + v_y \vec{N}^T \frac{\partial \vec{N}}{\partial y} + v_z \vec{N}^T \frac{\partial \vec{N}}{\partial z} \right) dx dy dz \cdot \vec{v}_z + \\ & \quad \int \int \int_{V^{(e)}} \vec{N}^T \frac{\partial \vec{M}}{\partial z} dx dy dz \vec{p} = 0 \\ & \int \int \int_{V^{(e)}} \vec{M}^T \frac{\partial \vec{N}}{\partial x} dx dy dz \vec{v}_x + \\ & \quad \int \int \int_{V^{(e)}} \vec{M}^T \frac{\partial \vec{N}}{\partial y} dx dy dz \vec{v}_y + \\ & \quad \int \int \int_{V^{(e)}} \vec{M}^T \frac{\partial \vec{N}}{\partial z} dx dy dz \vec{v}_z = 0 \quad (11) \end{aligned}$$

where $V^{(e)}$ is the volume of the element over which a numerical integration is performed. The matrixes from all of the elements were assembled into a large set of simultaneous equations and boundary conditions added so that a solution could be found using a frontal method.²² Necessary boundary conditions were applied to form a laminar flow pattern. The pressures was set at fixed high and low values at the two open ends of the channel to set up the required pressure gradient and the velocities were set as zero on the channel walls to define a no slip boundary condition. Where a boundary value was not defined for a field variable such as pressure on the walls of the channel or velocity at the open ends, a natural or no flux condition was assumed.

The velocities calculated from eqs 7 and 8 via FEM were then interpolated at the node positions of a new mesh of 8 noded linear hexahedral elements. This mesh was designed to solve eq 5 via FEM to find the concentration distribution C . The C field was approximated as the summation of 8 linear interpolation functions $M_i(x,y,z)$

$$C(x,y,z) = \sum_{i=1}^8 M_i(x,y,z) C_i \quad (12)$$

where C_i is the concentration of reactant at the i th node of each

element. Using the Galerkin Residual approach again, eq 5 was reduced to a matrix equation for each element (equ 13) and the assembly of all of the equations was solved with appropriate boundary conditions applied on the WE surface and the channel inlet

$$D \int \int \int_{V^{(e)}} \left(\frac{\partial \vec{N}^T}{\partial x} \frac{\partial \vec{N}}{\partial x} + \frac{\partial \vec{N}^T}{\partial y} \frac{\partial \vec{N}}{\partial y} + \frac{\partial \vec{N}^T}{\partial z} \frac{\partial \vec{N}}{\partial z} - v_x \vec{N}^T \frac{\partial \vec{N}}{\partial x} - v_y \vec{N}^T \frac{\partial \vec{N}}{\partial y} - v_z \vec{N}^T \frac{\partial \vec{N}}{\partial z} \right) dx dy dz \vec{C} = 0 \quad (13)$$

The value for C at the inlet was set as the bulk value C^∞ and the value on the WE was calculated from the electrode voltage via eq 6. For the first iteration, this voltage was assumed to be ideal and uniform so that, for a desired voltage V , $E = V$ was applied at all points on the electrode surface. On subsequent iterations, however, E was found using the calculated ϕ field.

The third mesh constructed from linear hexahedral elements was used to solve for ϕ . The Galerkin residual technique was applied to solve eq 3 with boundary conditions applied on the WE and the counter electrode. On the WE, the electric field was specified using a Neumann or gradient type boundary condition derived from the current density values. These current densities were calculated from the C field via eq 4 by interpolating the first y derivative of C at the position of each node on the electrode surface.

On the counter electrode a Dirichlet boundary condition was applied with an initial value of $\phi_C = -V$ where V is the desired voltage at the WE, assuming the potential of the WE itself to be zero by definition. The conductivity was assumed constant for the whole solution, implying that the reactive species C does not contribute significantly to the solution's charge carrying ability. The change in conductivity due to the nonuniform concentration of reactant is something that could be added to the simulation in the future.

To simulate the function of a potentiostat, the FEM solution of ϕ was repeated a number of times with eq 14 applied after each iteration. This was done until the value of ϕ_C converged to a good degree of precision

$$(\phi_C)_{i+1} = (\phi_C)_i - ((\phi_R)_i + V) \quad (14)$$

where ϕ_R is the potential on the RE and i is the iteration number. In most cases, convergence was achieved after one iteration as the value did not change on the second iteration by more than 0.1 mV.

The potential distribution ϕ was then used to recalculate the C field and produce a new set of current densities on the WE. This process was repeated until the total current was converged to less than 0.01% for each point on the current–voltage curve.

FEM Mesh

The fluid dynamic mesh of the MECD device consisted of an array of 12 by 6 by 4 elements in the x , y , and z directions, respectively. The grid was expanded in the x direction from $x = 0$ to $100 \mu\text{m}$ with a first element size of $5 \mu\text{m}$ because this was the region of most curvature in the velocity profile. From $x = 100 \mu\text{m}$ to L_x a uniform element size was used to fill the remaining space. A uniform element size was also used in the y and z directions.

The meshes for the concentration and electric field calculations were exponentially expanded from the edges of the electrode in the x and z directions and in the y direction from the electrode surface to the channel wall opposite as reported previously.^{16,14} A first element size of $0.1 \mu\text{m}$ was found to be

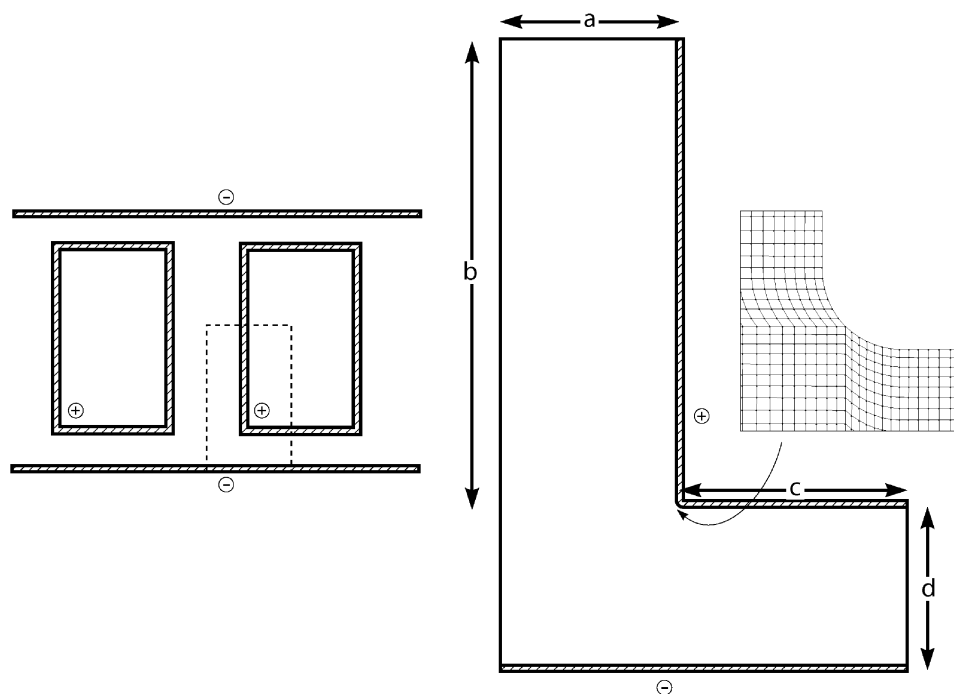


Figure 2. Geometry of the potential distribution model used for code validation. The symmetry of the model is shown on the left, and the mesh near the rounded corner is drawn in detail on the right.

acceptable for moderate flow rates. For the electric field calculation, an additional expanding region was also added around the position of the RE as this was required for good convergence. Typically of the order 20 by 15 by 40 elements were used in the x , y , and z directions, respectively. The codes were written in C++ and run on a COMPAQ Alpha XP1000 workstation.

Results and Discussion

The FEM code was validated by comparing the output against problems for which either an analytical solution is known or some previous numerical results have been obtained by other codes. The first step was to check the validity of the potential distribution calculation in isolation of any mass transport processes. This is valid in cells where there are no significant gradients of reactant concentration near the surfaces of the electrodes due to adequate stirring of the solution. In this case, diffusion can be ignored and a primary current density distribution can be obtained by solving the Laplace equation. The problem considered was a geometry first simulated in one of the earliest numerical current density distribution calculations by Klingert and co-workers.²⁴ The cell consists of an L shaped region of solution bounded on one side by a cathode and on the two concave edges by an anode. This represents one corner of an electrode in an array of rectangular electrodes as shown in Figure 2. A potential difference of 1.0 V was applied between the two electrodes, and other edges were set as insulators or planes of symmetry. The corner was rounded with a radius of $d/20$ to prevent a singularity in the current distribution. Conductivity was set as $\kappa = 1.0 \Omega^{-1} \text{ cm}^{-1}$, and the dimensions a , b , c , and d were set as $a = 1.0$, $b = 4d$, $c = 2d$ and various values of d were used in the range $1/2 \leq d \leq 4$. The anode current density, relative to that at the extreme right of the L shape, was plotted against the distance from the corner position as done by Klingert et. al. As can be seen in Figure 3, the previous FDM results are in good agreement with the FEM code used here for a range of geometries.

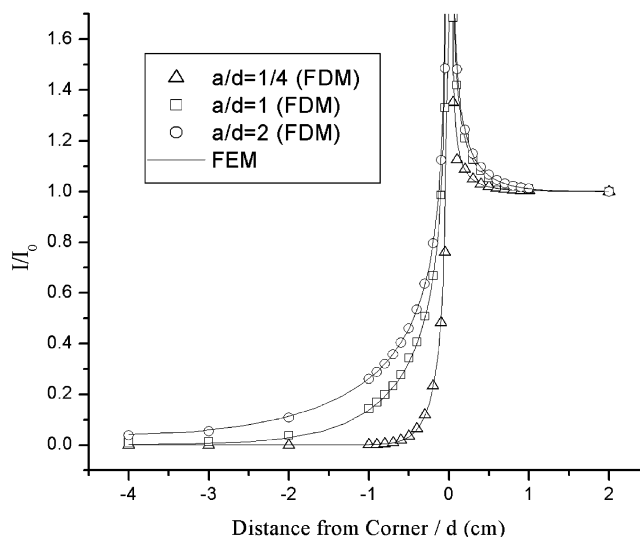


Figure 3. Comparison of the current density distribution with varying ratios of a/d for the previous FDM code and the FEM code used here.

The Navier Stokes and convection-diffusion parts of the code were similarly tested in isolation of any potential distribution effects by considering the case of a rectangular channel electrode. A 3d velocity profile was calculated for a channel of height $50 \mu\text{m}$ and a range of widths between 100 and $500 \mu\text{m}$. A rectangular electrode of various lengths was placed in the center for the full width of the channel (Figure 1). The total electrode current was plotted as a function of $(\text{volume flow rate})^{1/3}$ for flow rates in the range 0.001 – $0.01 \text{ cm}^3\text{s}^{-1}$. This showed a linear relationship as expected and was in good agreement with the semiempirical Levich equation and experimental results which are published previously.¹⁶

As a further validation, a combined potential distribution and mass transport simulation was done with a geometry for which a similar study has been conducted by Coles et al.⁶ Their cell consisted of a channel of height $400 \mu\text{m}$ and width 6 mm with

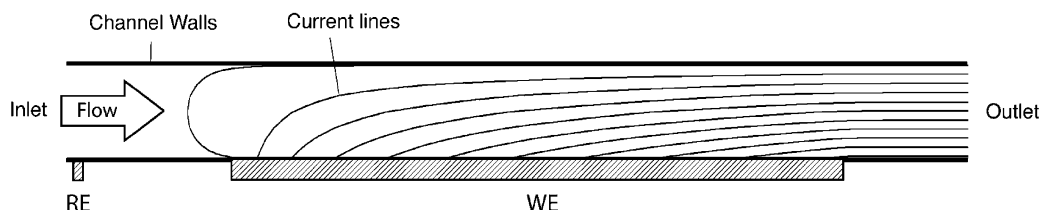


Figure 4. Current lines from a channel electrode derived from the potential distribution and mass transport calculation, showing the extent to which current travels up stream.

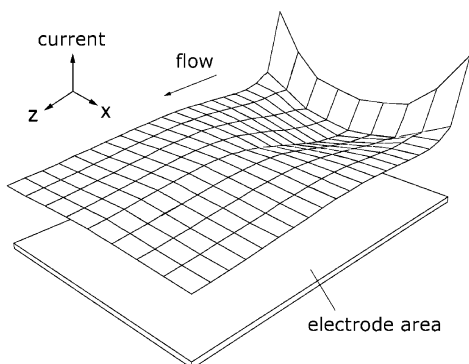


Figure 5. Current density distribution on the working electrode with the x -axis diffusion ignored at a potential of $E_0 = 17.5$ mV and electrode dimensions 3.39 mm wide by 4.14 mm long.

an electrode length of 4.14 mm and width 3.39 mm in the center of the channel. This was duplicated here by dividing the cell in two along the plane of symmetry and simulating one-half with a mesh of elements of height $400\text{ }\mu\text{m}$, length 2.0 cm and width 3 mm. The reference was placed at $z = 0$ for the whole channel height. The WE was between $z = 0.3$ and 0.714 cm on the bottom of the cell and the counter was placed at $z = 2.0$ cm.

A 3d mesh was used to solve for ϕ via FEM as described above; however, as the Coles paper only considered transverse mass transport, along the length of the electrode, the C field was calculated with a set of 2d simulations in the y - z plane to effectively remove diffusion of material in the x direction. These used a similar FEM formulation as described above but used 4 noded rectangular elements.^{23,25}

The potential V was then scanned between -0.2 V and $+0.2$ V in 200 increments and the steady-state current was converged for each step. Other parameters were $E_0 = 0$ V, $T = 289$ K, $C^\infty = 2.1$ mM, $n_e = 1$, and $\kappa = 0.00884\text{ }\Omega^{-1}\text{cm}^{-1}$. Figure 4 shows the simulated current lines in the y - z plane at the center of the channel which were plotted from the ϕ field. Agreement was found between the shape of the Tafel slope analysis predicted by the two approaches for a range of different limiting currents. Figure 5 shows the simulated current distribution over the surface of the WE at a potential of $E_0 = 17.5$ mV. This demonstrates the same increase in current at the two leading corners of the electrode due to the passage of current around the sides of the channel and a minimum in the current density near the middle of the electrode.

To validate the full 3d code, the channel cell simulation described above was repeated this time using a 3d mesh for both the C and ϕ fields. Figure 6 shows the current density distribution over the WE. This shows the same current peaks at the two leading corners and a minimum near the center of the electrode as well as an additional increase in the current density along the two outside edges of the electrode which is seen in this model but not the previous work and can be attributed to the diffusion to the electrode of reactive material in the x axis.

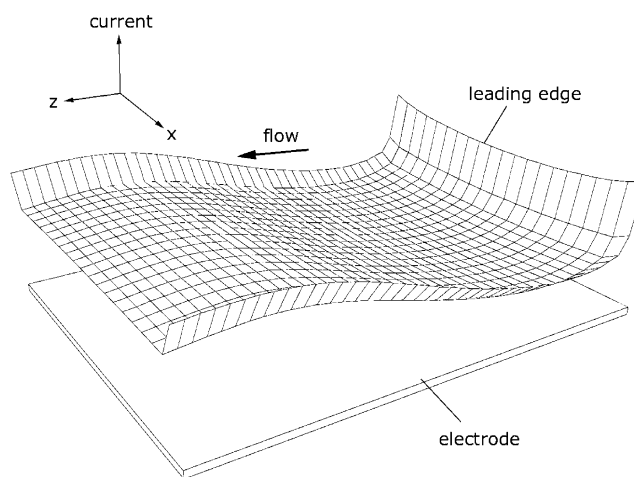


Figure 6. Current density distribution from the full 3d simulation at $E_0 = 17.5$ mV.

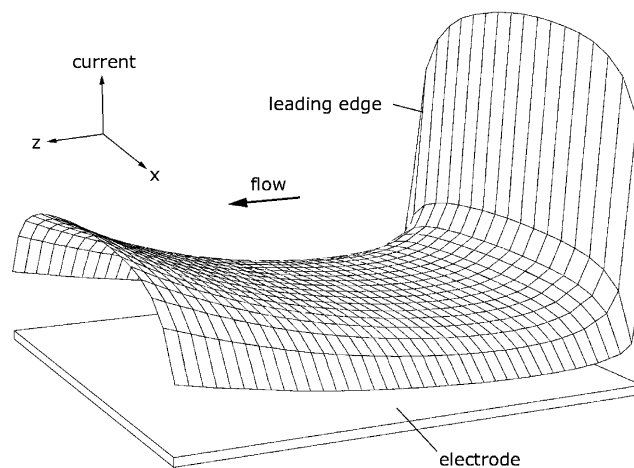


Figure 7. Current density distribution in a MEQR with the working electrode across whole channel width at $E_0 = 17.5$ mV and electrode dimensions $100\text{ }\mu\text{m}$ by $100\text{ }\mu\text{m}$.

Microreactor cell designs were then studied as described above with dimensions of $50\text{ }\mu\text{m}$ high by $100\text{ }\mu\text{m}$ wide with an electrode placed across the whole channel width. As before, the voltage was scanned between over potentials of -0.2 to $+0.2$ V for a range of electrolyte conductivities between 0.001 and $0.01\text{ }\Omega^{-1}\text{cm}^{-1}$ and Tafel slope plots were calculated for each. Figure 7 shows the current density distribution over WE at $V = E_0 = 17.5$ mV. This can be seen to differ significantly in shape from that of the central channel electrode in Figure 6. There is no longer a peak in current density at the leading corners of the electrode but rather a drop in current density along the edges of the electrode attributable to the fact that there is reduced solution flow near the channel walls and that there is no longer a path for the current to travel around the sides of the electrode. The microchannel simulations show a smaller positive and negative error in the Tafel slopes (Figure 8) even

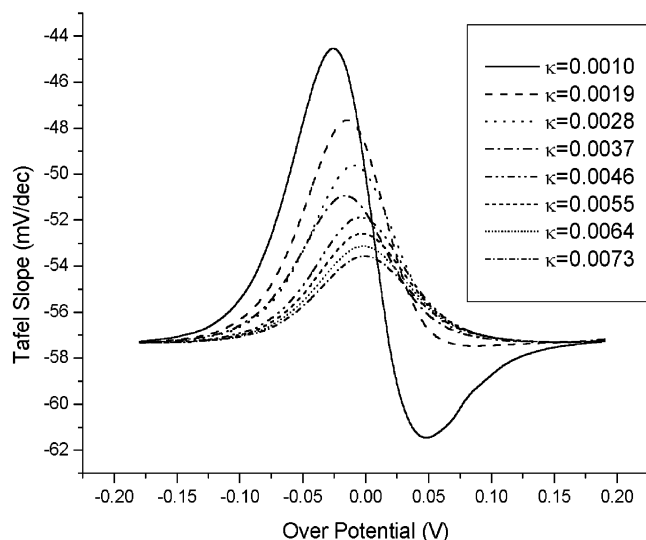


Figure 8. Tafel slope for a MECR at varying solution conductivities for a limiting current of $0.634 \mu\text{A}$.

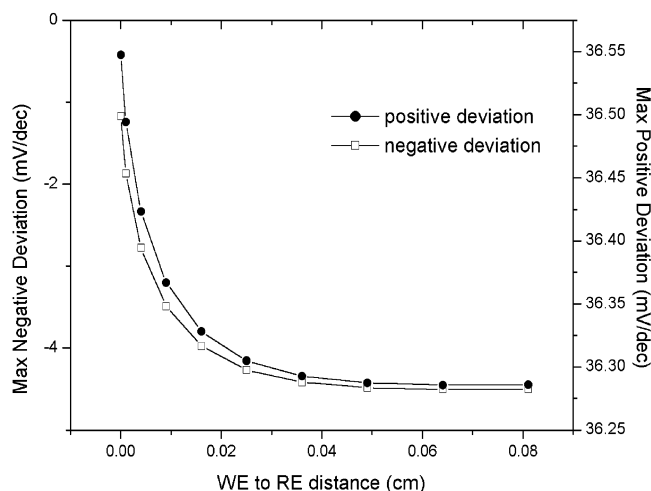


Figure 9. Maximum positive and negative deviation from -57.37 mV/decade of the Tafel slope plotted against the distance of the RE behind the WE for the macro channel at a limiting current of $904.6 \mu\text{A/cm}$ (electrode width).

with very low conductivity solutions due mainly to the smaller currents being passed.

Reference Position

To study the effect of different reference positions on the current voltage curves, the model was reduced to 2 dimensions by considering a slice in the y - z plane at the center of the macro channel cell described above. This was done to simplify the model by considering the case of a thin, infinitely wide channel. The RE was idealized as an infinitesimally thin strip on the bottom of the cell by using a single node in the FEM simulation. This represents a geometry sometimes used in channels cells where the reference is made from a strip of gold or silver a few μm in length.^{26,27} Tafel slope plots were simulated for RE positions at varying distances behind the leading edge of the WE with the current kept constant. The voltage was scanned between $E_0 - 0.2 \text{ V}$ to $E_0 + 0.2 \text{ V}$ as before and Tafel slopes were calculated for each reference position. Figure 9 shows the maximum positive and negative deviations in the Tafel Slope from the expected value of -57.37 mV/decade (16°C) plotted against the distance between the WE and the RE. The positive deviation showed only a small dependence on the position of

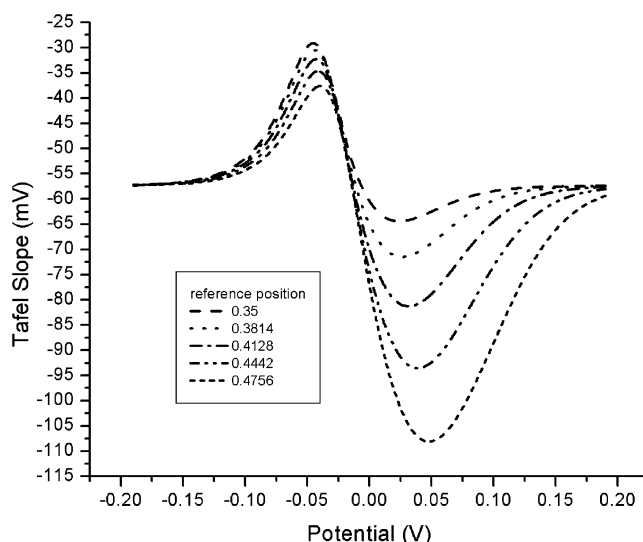


Figure 10. Tafel slopes for varying positions of the RE in front of the leading edge of the WE ($z = 0.3 \text{ cm}$) on the opposite wall of the channel at a limiting current of $488.5 \mu\text{A/cm}$.

the RE; however, the magnitude of the negative deviation was reduced significantly for distances shorter than $\sim 0.6 \text{ mm}$ such that it was smallest for lengths approaching zero. At larger displacements, the Tafel slope remained invariant as little current was passed through the solution at these more distant positions upstream of the WE.

The RE was then placed on the opposite wall of the channel, and simulations were carried out for RE positions between the start and end of the WE. This is analogous to the position of the RE often used in microdisk cells where a lugin probe is placed within close proximity of the center of the disk. Figure 10 shows the Tafel slopes for different positions above the WE. The negative deviation can be seen to increase rapidly with the distance of the RE from the leading edge compared with only a slight reduction in the positive deviation. This suggests that the best position for the RE is as close as possible to the leading edge of the WE.

Generator Collector Measurements

By placing a second working electrode (W2) in the cell downstream of the first (W1) with an offset potential, it is possible to drive the equilibrium of the reaction at W2 in the opposite direction to W1. This arrangement, sometimes referred to as a collector-generator cell allows, for example, the reoxidation of a species at W2 that has been reduced at W1. This system can be used among other things for studying the kinetics of second-order reactions by monitoring the exact amount of species that is re-oxidized. The problem encountered in channel cells is in choosing the correct offset potential for W2 because the potential difference between the solution and W2 is influenced by the solution's distribution of potential.

FEM simulations were set up as before with the reference at $z = 0$. The second working electrode was placed in the cell between 0.8 and 1.2 cm with the same boundary conditions as were applied to W1 but with an offset (V_{offset}) added to the electrode's potential. In Figure 11, I/I_0 is plotted against over-potential for a range of V_{offset} values, where I is the current on W1/W2 and I_0 is the limiting current on W1. The simulations reveal that at large over-potentials an oxidation will be performed on both W1 and W2. A reduction reaction on W2 can only be achieved if V_{offset} is chosen sufficiently large as expected. One effect of the potential distribution is that the

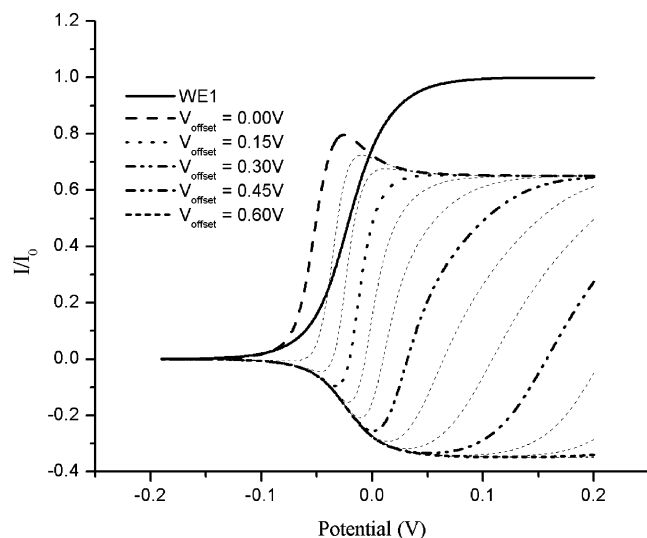


Figure 11. Current–voltage curves for a double working electrode channel cell with varying offset potentials (V_{offset}) between the two electrodes. Positive currents indicate an oxidation and negative currents a reduction. There is only one curve for WE1 as this was invariant with offset potential.

current through W2 with V_{offset} less than approximately 0.1 V rises faster than the current through W1 due to its closer proximity to the counter electrode. At higher over-potentials, W2 reaches a mass transport limited current which is lower than the current from W1 due to the reduced concentration of reactive species downstream.

Conclusions

A fully 3d finite element code has been developed which models both the mass transport and electric field in a micro-electrochemical reactor. The current–density distribution simulations can be used to predict the current–voltage response of the devices for low conductivity solutions. The simulations can also be used for the computer aided design of new reactor devices to help determine the best configuration for the counter, working, and reference electrodes. The effect of the reference electrode position on the current–voltage response for a channel cell has been investigated and the smallest error in the Tafel slope was found with the reference as close as possible to the leading edge of the working electrode. The effect of potential distribution on the potential of multiple working electrode systems has also been shown and revealed that careful choice of offset potentials between different working electrodes is required. The use of the finite element method allows for the modeling of curved surfaces and complicated geometries, which are often used in MECR devices. In the future, it would also

be of interest to include migratory mass transport effects to the model to improve accuracy and also allow the simulation of 3d electroosmotic driven fluid flow. The effects of reactant concentration on solution conductivity could also be added to improve the simulation.

Note Added after ASAP Posting. This article was posted ASAP on 6/17/2003. Changes have been made in refs 21, 22, and 23. The correct version was posted on 7/3/2003.

References and Notes

- (1) Dukovic, J. O. *IBM J. Res. Dev.* **1990**, *34*, 693–705.
- (2) Cooper, J. A.; Compton, R. G. *Electroanalysis* **1998**, *10*, 141–155.
- (3) Brett, C. M. A.; Maria, A. *Comput. Chem. Kinet.* **1986**, *26*, 355.
- (4) Brett, C. M. A. *Comput. Chem. Kinet.* **1999**, *37*, 573.
- (5) Coles, B. A.; Compton, R. G.; Spackman, R. A. *Electroanalysis* **1993**, *5*, 41–46.
- (6) Coles, B. A.; Compton, R. G.; Larson, J. P.; Spackman, R. A. *Electroanalysis* **1996**, *8*, 913–917.
- (7) Bard, A. J.; Faulkner, L. R. *Electrochemical Methods*; John Wiley & Sons: New York, 1980.
- (8) Theemsche, A. V.; Deconinck, J.; Bossche, B. V.; Bortels, L. *Anal. Chem.* **2002**, *74*, 4919–4926.
- (9) Ismagilov, R. F.; Kenis, P. J. A.; Stroock, A. D.; McDonald, J. C.; Stone, H. A.; Whitesides, G. M. *Abstr. Papers Am. Chem. Soc.* **1999**, *218*, 247-ORGN.
- (10) Manz, A.; Eijkel, J. C. T. *Pure Appl. Chem.* **2001**, *73*, 1555–1561.
- (11) Qin, D.; Xia, Y. N.; Rogers, J. A.; Jackman, R. J.; Zhao, X. M.; Whitesides, G. M. *Microsyst. Technol. Chem. Life Sci.* **1998**, *194*, 1–20.
- (12) Xia, Y. N.; Whitesides, G. M. *Angew. Chem.-Int. Ed.* **1998**, *37*, 551–575.
- (13) Aixill, W. J.; Fisher, A. C.; Fulian, Q. *J. Phys. Chem.* **1996**, *100*, 14067–14073.
- (14) Gooch, K. A.; Williams, N. A.; Fisher, A. C. *Electrochem. Commun.* **2000**, *2*, 51–55.
- (15) Fisher, A. C.; Gooch, K. A.; Henley, I. E.; Yunus, K. *Anal. Sci.* **2001**, *17*, 371–374.
- (16) Henley, I. E.; Yunus, K.; Fisher, A. C. *J. Phys. Chem. B* **2003**.
- (17) Stevens, N. P. C.; Hickey, S. J.; Fisher, A. C. *Anal. Quimica* **1997**, *93*, 225–232.
- (18) Stevens, N. P. C.; Fisher, A. C. *J. Phys. Chem. B* **1997**, *101*, 8259–8263.
- (19) Stevens, N. P. C.; Gooch, K. A.; Fisher, A. C. *J. Phys. Chem. B* **2000**, *104*, 1241–1248.
- (20) Fisher, A. C.; Compton, R. G. *J. Appl. Electrochem.* **1992**, *22*, 38–42.
- (21) Geankoplis, C. J. *Transport Processes and Unit Operations*; Allyn and Bacon Inc.: Boston, MA, 1983.
- (22) Taylor, C.; Hughes, T. G. *Finite Element Programming of the Navier–Stokes Equations*; Pineridge Press: Swansea, U.K., 1981.
- (23) Dhat, G.; Touzot, G. *The Finite Element Method Displayed*; Wiley-Interscience Pub.: New York, 1984.
- (24) Klingert, J. A.; Lynn, S.; Tobias, C. W. *Electrochim. Acta* **1963**, *9*, 297–311.
- (25) Zienkiewicz, O. C.; Taylor, R. L. *The Finite Element Method, The Basis*, 5 ed.; Oxford: New York, 2000; Vol. 1.
- (26) Yunus, K.; Rickson, S. A.; Fisher, A. C.; Henley, I. E.; Allsopp, D. W. E.; Ryan, T. J. *Electrochem. Commun.* **2001**, *3*, 455–459.
- (27) Yunus, K.; Marks, C. B.; Fisher, A. C.; Allsopp, D. W. E.; Ryan, T. J.; Dryfe, R. A. W.; Hill, S. S.; Roberts, E. P. L.; Brennan, C. M. *Electrochem. Commun.* **2002**, *4*, 579–583.